Experimental investigation of beam-ion losses induced by magnetic perturbations using the light ion beam probe technique in the ASDEX Upgrade tokamak

J.Galdon-Quiroga[1,2], L.Sanchis-Sanchez[3], X.Chen[4], G.Birkenmeier[2], K.Gage [5], P.Cano-Megias[6], J.Gonzalez-Martin[5], W.W.Heidbrink[5], O.Putignano[7], D.Ryan[8], G.Suarez Lopez[2], B.Tal[2], M.A.VanZeeland[4], E.Viezzer[1], M.Willensdorfer[2], the ASDEX Upgrade Team ‡ and the EUROfusion MST1 Team§

1 Dept. of Atomic, Molecular and Nuclear Physics, University of Seville, Avda. Reina Mercedes, 41012 Seville, Spain

2 Max Planck Institute for Plasma Physics, Boltzmannstr. 2, 85748 Garching, Germany

3 Dept. of Applied Physics, Aalto University, FI-00076, Aalto, Finland

4 General Atomics, San Diego, CA, United States of America

5 University of California, Irvine, CA, United States of America

6 Dept. of Energy Engineering, University of Seville, Camino de los Descubrimientos s/n, 41092 Seville, Spain

7 Dipartimento di Fisica 'G.Occhialini', Universita di Milano-Bicocca, Milano, Italy

8 CCFE, Culham Science Centre, OX14 3DB, Abingdon, United Kingdom

E-mail: `jgaldon@us.es`

Abstract.
The impact of externally applied magnetic perturbations (MPs) on fast-ion losses has been investigated by means of the light ion beam probe (LIBP) technique in the ASDEX Upgrade (AUG) tokamak. The LIBP technique allows to experimentally infer the fast-ion orbit displacement induced by MPs via first-orbit losses using scintillator based fast-ion loss detector (FILD) measurements. The fast-ion orbit displacement against different applied MP spectra has been studied. These shots were conducted in ELM mitigated H-mode plasmas. A rigid rotation of the MP coils was applied with a frequency of 1 Hz, with an n=2 configuration and changing the differential phase between the upper and lower set of coils ($\Delta\Phi_{ul}$) in a shot to shot basis. Beam sources Q7 (tangential) and Q8 (radial) were used to probe different fast-ion orbits with FILD1. The measured fast-ion orbit displacement ranges from 3 to 20 mm approximately, and no qualitative difference is observed between ions from beam sources Q7 and Q8. The minimum is found for a $\Delta\Phi_{ul} \sim 50^o$, which is shifted with respect to the minimum of the plasma boundary displacement, found at $\Delta\Phi_{ul} \sim 0^o$. A first attempt to validate the orbit following code ASCOT -including the plasma response calculated with the MARS-F code- against these experimental measurements is performed. While the dependence of the first-orbit fast-ion displacement with $\Delta\Phi_{ul}$ does not match the experimental measurements, these simulations do capture other features such

‡ See author list of H.Meyer et al., 2019 Nucl. Fusion **59** 112014
§ See the author list of B.Labit et al., 2019 Nucl. Fusion **59** 086020.

as the order of magnitude of the orbit displacement and the importance of the toroidal spectrum of the applied perturbation.

1. Introduction

In tokamak plasmas the so called high confinement mode (H-mode) [1] is one of the possible modes of operation candidates for future experiments such as ITER and, ultimately, for future fusion reactors as well. Inherent to the H-mode, edge localized modes (ELMs) [2, 3] appear in a cyclic fashion. These are thought to be peeling-ballooning instabilities driven by the steep pressure gradient and current density at the edge of the plasma [4], releasing particles and energy to the plasma facing components, and therefore leading to transient peaks of increased heat load. Based on scaling laws from current experiments, it is predicted that type-I ELMs will be untolerable for future reactors [5, 6, 7, 8].

Therefore, reliable mechanisms for ELM control need to be developed. Amongst these, the control of ELMs using externally applied magnetic perturbations (MPs) has been the subject of extensive studies in the past years (e.g. see [9] and references therein). Although there is not yet consensus on the physics mechanism leading to it, the mitigation and suppression of ELMs using MPs has been experimentally achieved in different machines such as AUG [10], DIII-D [11], KSTAR [12] and EAST [13] .

However, it has also been noted that the application of MPs can be detrimental for the confinement of fast-ions (FI). This has been reported in different experiments in ASDEX Upgrade [14, 15, 16], in DIII-D [17, 18], in KSTAR [19] and in MAST [20, 21]. This is an issue of concern since a good confinement of fast-ions, either from auxiliary heating systems or from nuclear reactions, is desirable to both ensure a good plasma heating and current drive efficiency, and to avoid excessive heat loads to plasma facing components. In fact, the impact of ELM Control Coils (ECC) on the confinement of NBI and alpha particle populations in ITER has been thoroughly investigated using codes such as OFMC [22, 23] and ASCOT [24, 25, 26, 27, 28]. These works show that ECCs can potentially lead to excessive fast-ion heat loads. Therefore, it is important to understand which are the physics mechanisms underlying the MP induced fast-ion transport, for two reasons: (a) to be able to make robust predictions for future devices and (b) to develop strategies for the optimization of the applied MP spectrum to simultaneously control ELMs while minimizing the impact on fast-ion confinement.

Unravelling the physics behind the mechanisms leading to fast-ion transport induced by externally applied 3D fields has been the subject of many numerical and theoretical studies in the past years[16, 18, 27, 29, 30, 31, 32, 33, 34, 35, 36]. However, it is a challenging task since it is a multidimensional problem dealing with the interaction of, in general, 5D FI distribution functions (three spatial coordinates, plus the energy and pitch angle of the particles) with 3D magnetic field topologies. Different mechanisms have been identified such as: transport due to the stochasticity of magnetic field lines [29, 32, 27], topological boundary crossings favoured by MP perturbations [31], or resonances between the FI orbits and the applied MP fields. The question of which of these mechanisms is the dominant one is difficult to answer since it depends on many different factors such as the characteristics of the fast-ion distribution function, the timescales of interest or the characteristics of the applied MP configuration.

Lately, special attention has been drawn to resonant-like mechanisms. In AUG, it was shown that there is a thin layer in the edge of the plasma that contains a large density of FI-MP resonances - dubbed edge resonant transport layer (ERTL) [16]. In general, both linear [30] and non-linear [16, 34] resonances need to be considered. When resonant transport is present, one has to distinguish between two cases: if there is phase-space resonance overlapping or not. The former leads to orbit stochasticity [32] and leads to diffusive like transport which scales as δB^2, while the latter leads to convective-like transport, scaling as δB. Whether one or the other case dominates depends strongly on the applied MP spectrum and background equilibrium, specially through the q-profile shear. For instance, it was found in simulations with EAST-like parameters that an n=1 MP perturbation leads to diffusive-like scaling of the loss power, while n=2 MP perturbation leads to convective-like scaling [33].

Since resonant-like processes are velocity-space dependent, differences in the behaviour of trapped and passing particles can be expected. Indeed, this has been observed in simulations where the fraction of loss power as a function of $\Delta\Phi_{ul}$ was found different for trapped and passing particles [32, 36], where $\Delta\Phi_{ul}$ is the differential phase between two sets of MP coils.In addition to the applied MP spectrum, it has been shown that also the (toroidal) phase between the MP field and the target FI distribution matters. This way, one can find regions of phase space where the fast-ions experience outwards or inwards radial transport [16, 35, 18].

It is also acknowledged that the inclusion of the plasma response to the perturbing fields needs to be included for an accurate prediction [16, 36]. The role of plasma response on the MP induced fast-ion transport is still a subject of study. The effect is twofold: on one side it can help to reduce losses by reducing the size of the edge ergodic layer induced by the MPs, while on the other hand it can also have detrimental effects on the resonant fast-ion transport channel, by amplifying specific components of the perturbed fields.

Motivated by previous experimental results at

AUG and DIII-D [16, 18] which relied on a limited number of discharges, in this work we provide a more systematic study of the dependence of fast-ion losses on the applied MP spectrum in AUG. The study is based on the application of the light ion beam probe technique using FILD measurements [37, 38, 39]. With it, we aim to provide experimental measurements of a specific observable such as the fast-ion orbit displacement induced by MP, which can be directly compared to simulations. In this way, the main goal of this paper is to provide experimental measurements that can serve as a testbed for the validation of our current numerical tools, therefore improving our confidence when making predictions to future machines.

The paper is organized as follows: in Section II we present the experimental setup. A special focus is put on the description of the light ion beam probe technique and its generalization when applied to MPs. In Section III we describe the results from experiments at AUG, mainly: the impact of the applied MP spectrum on first-orbit fast-ion losses. The impact of 3D density perturbations on our experimental FILD signals is discussed. In section IV these are compared to ASCOT simulations. In section V we present our conclusions and discuss some considerations regarding strategies for the optimization of MP configurations in terms of fast-ion confinement for future devices.

2. Experimental setup and methods: the light ion beam probe technique

The experiments described in this work are designed to apply the so called light ion beam probe technique (LIBP) by using a scintillator based fast-ion loss detector (FILD1). The LIBP technique [38, 39], was first applied in the DIII-D tokamak to study fast-ion losses induced by Alfven Eigenmodes (AE). However, its application is not limited to the study of AEs. In general, to apply this technique three main ingredients are needed:

(i) An NBI source that puts first-orbit losses in the FILD detector. We will refer to these as "probe beams" or "probe NBI" for the remaining of the manuscript.

(ii) Ensure the first-orbit loss character of the losses. In practice this is done by including notches in the probe beam's waveform.

(iii) An instability that modulates the FILD signal.

In the case of MPs, this recipe can be implemented experimentally by applying a rigid rotation of the MP field, while keeping constant the MP spectrum.

As introduced by X.Chen et al [39], the modulation of the FILD signal can be used to infer the fast-ion orbit displacement due to the corresponding instability, following the formula:

$$\xi = \frac{\Delta F}{F} \cdot L_i \tag{1}$$

where ξ is the orbit displacement, ΔF is the amplitude of the modulated FILD signal, F is the level of the FILD signal in the absence of instabilities and L_i is the ionization scale length at the birth position of the fast-ions probed by FILD. In this work, the ionization scale length can be approximated by the density scale length (L_{n_e}) as in [39].

However, Eq.1 is derived upon the assumption that the ionization scale length at the birth position of the probing beams remains unchanged. In our case, this might not necessarily hold, since it is well known that MPs perturb the flux surfaces in the plasma edge. In such a case, we need to generalize Eq. 1 to include a correction factor due to plasma boundary displacements (PBD) (see Appendix):

$$\begin{aligned} L_{n_e}(\vec{r}_{birth}) \cdot \frac{F - \langle F \rangle}{\langle F \rangle} - \sum_{n=1}^{all} \xi_n^{pl} \cdot \cos(n\phi + \alpha_n) = \\ = \sum_{n=1}^{all} \xi_n^{FI} \cdot \cos(n\phi + \beta_n) \end{aligned} \tag{2}$$

where L_{n_e} is the density scale length $\frac{n_e}{\nabla n_e}$ at the birth position of the probing ions, F is the FILD signal, $\langle F \rangle$ is the mean value of the FILD signal over a full modulation period, ξ^{pl} is the plasma boundary displacement, ξ^{FI} is the fast-ion orbit displacement induced by the MPs, ϕ is the toroidal coordinate, and α and β are included to take into account the phase between the applied perturbation and the induced plasma boundary displacement and fast-ion orbit displacement which, in general, are not the same. The need of this generalization is justified in subsection 3.2. In Eq.2 the terms in the left hand side can be extracted from experimental measurements. Then, the term in the right hand side can be inferred.

In AUG the set of MP coils consists of two sets of 8 coils, one above and one below the midplane, capable of providing MP spectra with toroidal mode numbers $n = 1, 2, 3, 4$. The main diagnostics used in this work are the fast-ion loss detector [40, 41], FILD1, which is mounted on the midplane manipulator at $z = 0.32$ m and $R = 2.185$ m, and the lithium-beam diagnostic (Li-BES) [42, 43]. Figure 1 shows the experimental setup in AUG. In (a) a poloidal cross section of AUG is shown, where the equilibrium is illustrated. These experiments were carried out in a lower single null configuration, with a low average (upper and lower) triangularity of $\delta \sim 0.065$. The main diagnostics relevant for this work are shown in Figs.1 (a) and (b).

The injection geometry of beam sources Q7 and Q8 are plotted in red and blue respectively. The insertion geometry of FILD1 is shown in black, the injection geometry of the lithium beam is shown in green, and the interferometer chords used for the measurement of the core and edge line averaged densities are shown in black dashed lines.

3. Effect of the poloidal spectra on first-orbit fast-ion losses in ASDEX Upgrade

These experiments were carried out in H-mode deuterium plasmas, with a plasma current of 0.8 MA and magnetic field of -1.8 T, corresponding to an edge safety factor of $q_{95} = 3.85$, a core and edge line averaged density of $\sim 4.4 \cdot 10^{19}\ m^{-3}$ and $\sim 2.5 \cdot 10^{19}\ m^{-3}$ respectively, both edge electron and ion collisionalities $\nu \leq 0.5$, a $Z_{eff} \sim 1.4$, and 2.7 MW of ECRH power. An example is shown in Fig.2 for AUG shot 34597. A total NBI power of 5 MW was applied, which included beam source Q3 for diagnostic purposes, and phases with beam sources Q7 and Q8 (deuterium), both with a main injection energy of $\sim 93keV$, corresponding to a more tangential and radial injection geometry respectively. The probe beam is depicted in red Fig.2 (a). These two are used as fast-ion probing beams in these experiments. The shots included phases of 2s where a rigidly rotating MPs with a fixed differential phase between the upper and lower MP coils ($\Delta\Phi_{ul}$) were applied, with a rotation frequency of 1 Hz (in almost all shots) and a toroidal mode number $n = 2$. This is illustrated by the blue timetrace in Fig.2(c). In grey, the divertor shunt current is plotted which is used as an ELM monitor. It can be seen that, when the MPs are switched on, there is a slight density pump-out together with ELM mitigation. In order to explore the impact of different MP spectra, the $\Delta\Phi_{ul}$ was changed in a shot-to-shot basis. The database of shots carried out in AUG is summarized in Table 1. All these shots correspond to MP ELM mitigated plasmas.

3.1. Data analysis of Lithium-beam signals

We first discuss the data analysis of the lithium-beam (Li-BES) diagnostic signals. This data is used to (a) estimate the density scale length at the birth position of the probe beam (i.e. this is needed to evaluate the first term in the left hand side of Eq.2), and (b) to infer the plasma boundary displacement (PBD), following the same technique as in [44] (this is needed to evaluate the second term in the left hand side of Eq. 2).

We first focus on the calculation of the density scale length. The birth position of the probe fast-ions is in the separatrix - near SOL region. In this region, it has been shown for AUG that the density profile fits well to an exponential decay [45]. Since the application of the MPs strongly influences the shape of the edge density profile, both its magnitude and gradient, the use of the density profile prior or after the application of the MPs was discarded. Instead the following approach was followed: since the diagnostic lines of sight are fixed, and the plasma boundary shifts during the rigid rotation of the MPs, the time point corresponding to the mean density profile position ($t_{profile}$) was found by looking at the evolution of the density at a fixed diagnostic channel. Then, the density profile at this time point was used to calculate the density scale length. An example of the measured profile and corresponding exponential fit is illustrated in Fig.3 (a) for AUG shot 34597 in a time window between 2.5 and 2.6 s. In Fig.3 (b) the measured L_{n_e} is shown as a function of $\Delta\Phi_{ul}$. In all cases L_{n_e} is around 2 cm.

On the other hand, the plasma response has been evaluated in terms of the plasma boundary displacement measured close to the midplane, similar to the analysis carried out by M.Willensdorfer et al [44]. The technique consists in following iso-density layers along the diagnostic lines of sight during the MP rigid rotation cycles. This is illustrated in Fig.4 (a) for AUG shot 34597. The experimental signal is then fitted (blue line) to a function of the form:

$$f = A_0 + B \cdot t + C \cdot t^2 + \sum_{n=1}^{n=4} A_n \cdot \cos(n\omega t + \phi_n) \quad (3)$$

where n is the toroidal mode number of the perturbation, ω is the modulation frequency, which in our case corresponds to $\omega = \frac{2\pi}{T_{MPs}}$, being T_{MPs} the period of the MP rigid rotation, t is the time and ϕ is the phase. The B and C coefficients are included to account for possible slow time evolution in the density profile but are found to be always close to zero. From this fit, we are able to extract the amplitudes associated to the different components of the perturbation via the coefficients A_n. In all cases the dominant one is the $n = 2$ component.

The plasma boundary displacement as a function of $\Delta\Phi$ is shown in Fig.4 (b). Here, the $n = 0$ contribution of the plasma control system (PCS) has been taken into account in the analysis following the

‖ In the shots marked with a star the polarity of one of the lower MP coils was reversed with respect to the target configuration. This lead to a spectral leakage of the effectively applied MP configuration, mainly into the n=1 component. Since this could have a potential impact on the fast-ion geometrical resonances, it was decided to repeat these shots. However, the results from these shots are retained and presented in this paper as well. No significant difference was observed, within experimental errorbars, from the shots performed with the right MP configuration.

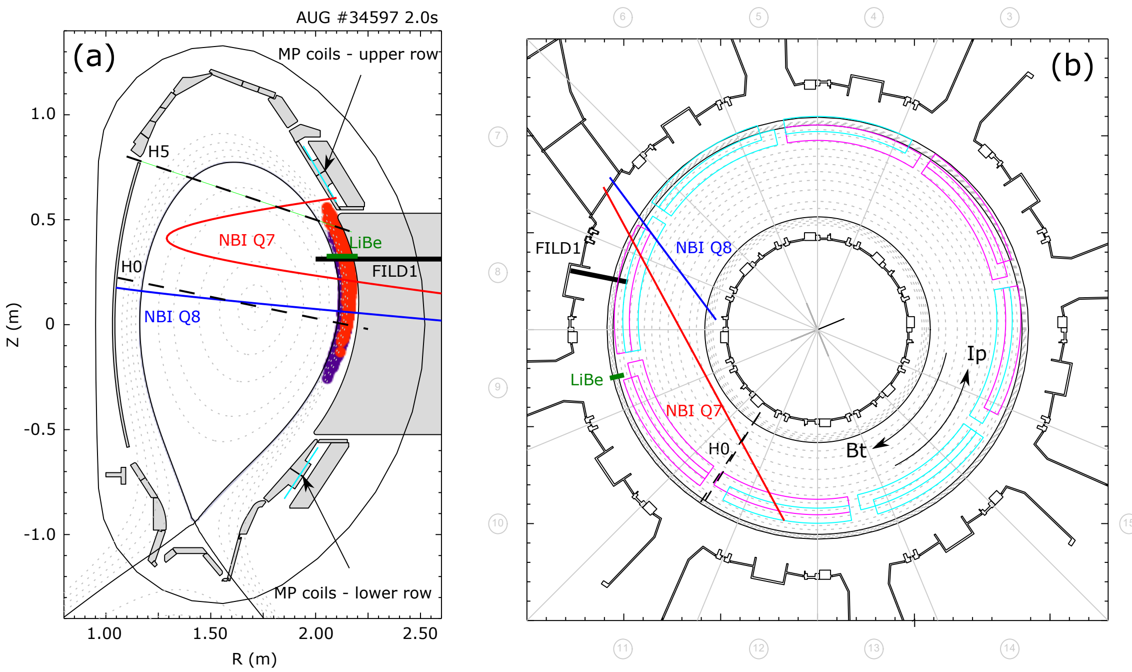

Figure 1. (a) Poloidal cross section of AUG. The main elements relevant to this study are highlighted. In blue and red, the NBI sources Q7 and Q8 injection geometry is shown. In black, the manipulator of the FILD1 diagnostic is indicated. In green, the injection geometry of the Li-BES diagnostic is shown. In cyan and magenta, the position of the upper and lower set of MP coils are plotted. The dashed black lines represent the core and edge interferometer chords. The red and blue dots represent the position of markers representing NBI ions from sources Q7 and Q8 which are lost to FILD1 in the simulations. (b) The toroidal projection of AUG, showing the same elements as in (a).

Shot	$\Delta\Phi_{ul}$	f (Hz)	NBI sources	$\langle n_e \rangle_{edge}$ $[10^{19}\ m^{-3}]$	$\langle \beta_n \rangle$
34584	42.7	4	7,8	1.99	2.52
34587	44.83	1	7,8	1.97	2.37
34597	-120.21	1	8	2.37	2.37
34598	-120.21	1	7	2.17	2.30
34599	-50.62	1	7	2.43	2.66
34601	-50.62	1	8	2.54	2.44
36396*	119.46	1	7,8	2.01	2.05
36398*	-0.5	1	7,8	2.27	2.41
36548*	159.48	1	7,8	1.95	1.99
36551*	-160.57	1	7,8	2.68	2.22
37619	-160.57	1	7,8	2.61	2.16
37620	119.46	1	7,8	2.59	2.17
37621	159.48	1	7,8	2.69	2.15
37622	159.48	1	7,8	2.69	2.14

Table 1. Overview of the analyzed shots at AUG ‖.

same method as the one described in [44]. The same qualitative dependency is found in these experiments as in the work by Willensdorfer et al [46], although a slightly larger displacement is measured, which could be attributed to the lower rigid rotation frequency in these experiments (1 Hz) compared to those ones (3 Hz), leading to a smaller attenuation of the applied magnetic perturbations due to the screening by passive conducting structures that are close to the MP coils. It can be observed that the minimum of the plasma boundary displacement sits at $\Delta\Phi_{ul} \sim 0^o$. The reason for the larger spread of the data at $\Delta\Phi_{ul} = 120^o$ and 160^o is likely the worse quality of the LiBe signal for those shots.

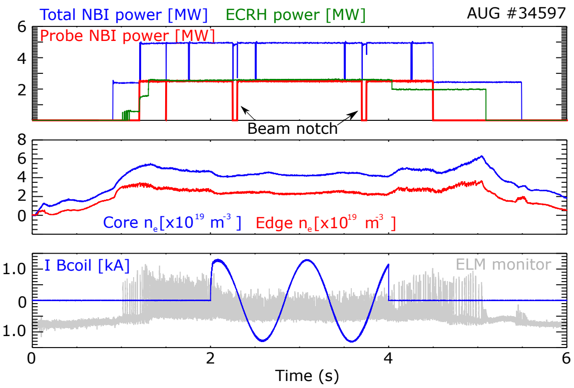

Figure 2. Overview of shot 34597 in AUG. (a) Total NBI power in blue, probe beam power (NBI Q8 in this case) in red, and ECRH power in green. (b) Core (blue) and edge (red) line averaged densities. (c) Timetrace of the current from MP coil "IBl6", in blue, and divertor shunt current, in grey, which is used as an ELM monitor.

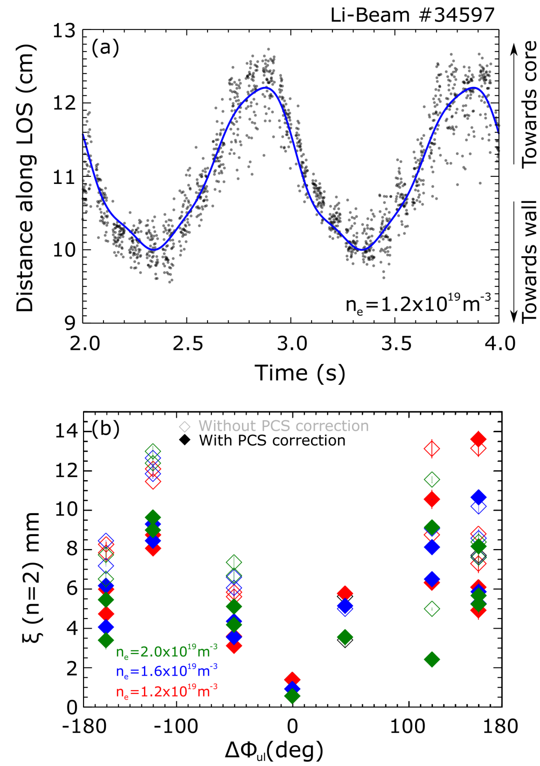

Figure 4. (a) Li-BES measurements of the iso-density layer corresponding to $n_e = 1.2 \cdot 10^{19}$ m^{-3}. (b) Measured n=2 component of the PBD as a function of $\Delta\Phi_{ul}$. In this case three different iso-density layers are shown: $n_e = (1.2, 1.6, 2.0) \cdot 10^{19}$ m^{-3}

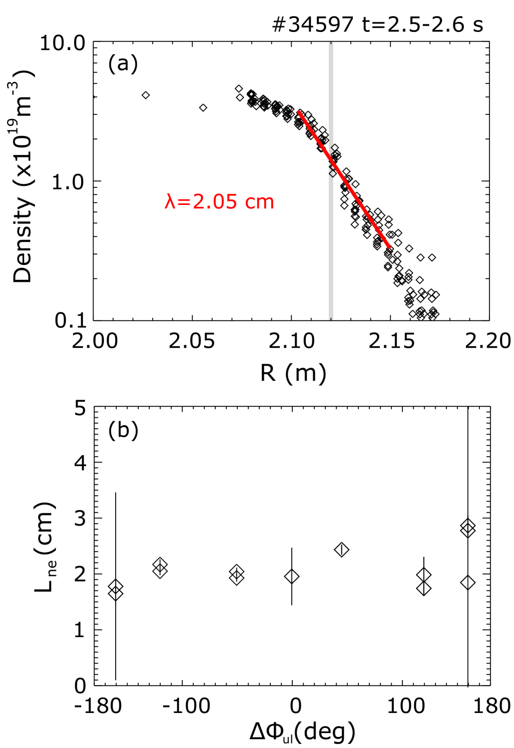

Figure 3. (a) Density profile measured by Li-BES diagnostic in shot 34597 in the time interval t=[2.5-2.6] s, and the corresponding exponential fit. (b) Measured density scale length as a function of $\Delta\Phi_{ul}$

3.2. Impact of density perturbations on fast-ion loss modulation

As mentioned in a previous subsection, during the application of the rigidly rotating MPs the plasma boundary is shifted, leading to an effective shift of the density profile, and therefore a modulation of the L_n at the birth position of the FI orbits. This motivates the question whether the modulation in the FILD signal is then dominated by the modulation of L_n rather than by a change in the FI orbit. In the case of DIII-D experiments, this question was addressed by M.VanZeeland et al [17], where simulations had shown that the modulation of the FILD signal considering only the 3D density perturbations was negligible compared to the orbit displacement effect.

In the case of AUG, a similar approach was followed and ASCOT [47] simulations were carried out which consisted in the following: first, the the BBNBI module within ASCOT is used, which calculates the NBI birth distribution by taking into account the beam properties (injected species, energy, geometry and power), the plasma parameters (density, temperature, impurities) and the relevant reaction rates in the ionization process. Then these NBI ions are followed until they hit a wall component or they complete a full poloidal transit. Therefore, long time scale losses are discarded. The same simulation is repeated but shifting radially the kinetic profiles ± 1 cm, as measured in the experiment. The orbit following is done in a fixed 3D magnetic equilibrium configuration, to isolate the effect of the kinetic profiles alone while having a perturbed 3D equilibrium. This is illustrated in Fig.5 (a), where the equilibrium density profile (in black) was artificially shifted by ± 1 cm, as observed in the experiment. A realistic 3D wall is used, which also includes a realistic 3D model of the FILD probe head, which is placed at the same radial position as in the experiment. The strike-points in the FILD probe head are collected for each simulation. The results are shown in Fig.5 (b) for NBI source Q7 (in blue) and Q8 (in red). It can be seen that the expected FILD signal can change by up to 50%. This is consistent with a simple estimation which follows from Eq.2 by neglecting the term in the right-hand side of the equation, and taking ξ^{pl} and $\frac{\Delta F}{\langle F \rangle}$ from the experimental measurements:

$$\frac{\Delta F}{\langle F \rangle} \sim \frac{\xi^{pl}}{L_{n_e}} \sim \frac{10mm}{20mm} = 0.5 \tag{4}$$

Therefore, we conclude that the impact of the 3D density profile perturbation induced by the MPs need to be taken into account in the analysis of the AUG experiment.

In addition, Fig.5 (c) shows the pitch angle of the fast-ions which are lost to the FILD probe head, from NBI source Q7 (in blue) and Q8 (in red). Here we have defined the pitch angle as $\eta = \frac{v_{||}}{v_{tot}}$, where $v_{||}$ is the component of the velocity parallel to the magnetic field and v_{tot} is the total velocity of the particle, with the sign relative to the plasma current direction. The lines represent the FILD measurement, while the histogram represents the result from ASCOT simulations. A good agreement is found, although there is a slight systematic shift of the centroid of the distributions of $\sim 4^o$. In Fig. 1 (a), the birth position in the poloidal plane of the fast-ions which are lost to the FILD probe head in the ASCOT simulation, is represented by the blue (Q7) and red (Q8) dots. It can be seen that they are all coming from a radial region around the separatrix - SOL. This is consistent with calculations done by tracking the ions backwards from the FILD probe head using the experimentally measured energy and pitch angle.

3.3. Data Analysis of FILD signals

We now focus on the analysis of the FILD signals. Only measurements from FILD1 are considered, and not from other FILDs, since due to technical reasons

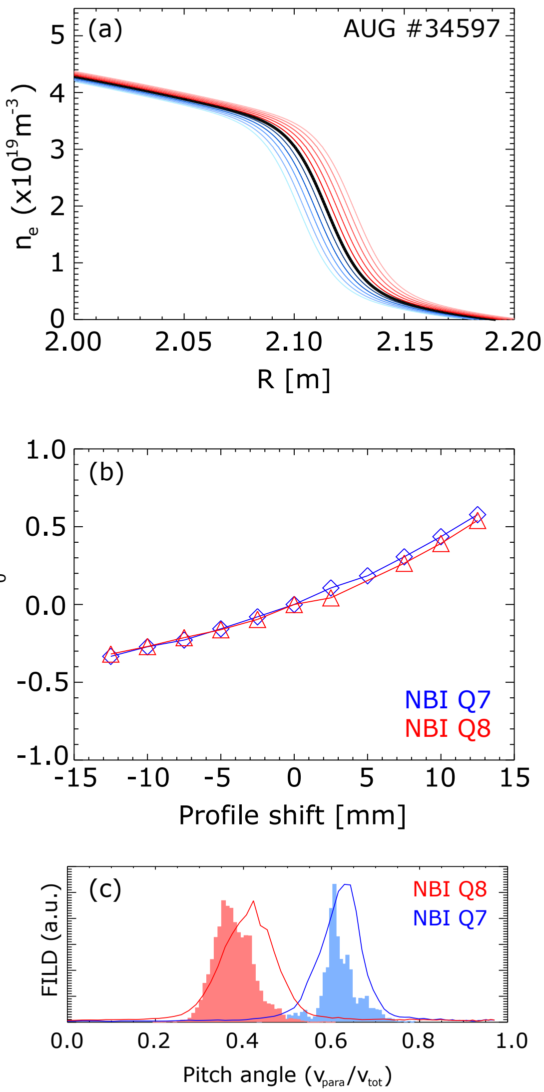

Figure 5. (a) Input density profiles used in ASCOT simulations to evaluate the effect of 3D plasma boundary displacement. (b) Fraction of lost fast-ion power collected at the synthetic FILD probe head as a function of the profile shift, with respect to the equilibrium case. (c) Pitch angle of the NBI Q7 (in blue) and Q8 (in red) ions lost to the FILD probe head. The lines represent the FILD measurement, while the histogram represent the results from ASCOT simulations.

only FILD1 measurements were possible in all the shots considered. Since the AUG experiments were carried out in H-modes, a filtering of the ELMs from the FILD signal was needed. This is illustrated in Fig.6 (a) for the case of AUG 34597, corresponding to the probe beam Q8. The raw FILD signal is plotted in grey. Once the ELMs are filtered, we are left with the slow (1 Hz) modulation of the FILD signal due to the impact of MPs, represented by the black dots. Again, in this case we fit this signal (blue line) using a function of the form shown in Eq.3, from which we can extract the modulation amplitudes from the different n components, which are needed for the application of the LIBP technique.

It can also be seen here the inclusion of 50 ms notches in the probe beam, intended to assess the first orbit loss character of these measurements. The fast acquisition system of the FILD detectors (a set of photomultipliers) was used to assess this, as illustrated in the figure insert. The FILD signal is observed to decay within $\sim 20\,\mu s$, corresponding to an orbit bounce time approximately. It can also be seen that in addition to the applied dominant $n = 2$ component, other components such as the $n = 4$ and $n = 6$ show up. Of special importance is the latter, which appears due to the fact that having only a limited number of MP coils in AUG ($n_{coils} = 8$ per row), the achieved spectrum is not a pure n=2, but an additional component appears as $n_{alias} = n_{coils} - n_{MP}$.

In Fig.6 (b) and (c) the measured modulation of the FILD signal $\Delta F/F$ as a function of the applied MP spectrum $\Delta\Phi_{ul}$ is shown for the extracted $n = 2$ and $n = 4, 6, 8$ components respectively. Both results, for probe beams Q7 and Q8 are shown. Several observations can be made from this plot already. First, that despite additional mode numbers show up in the FILD signal, the $n = 2$ component is clearly dominant. Second, that within errorbars, no clear difference is observed between probe beams Q7 and Q8. It could also be that the scan in $\Delta\Phi_{ul}$ is not fine enough to detect possible differences. Third, at this stage, it seems that the minimum in the FILD modulation sits at $\Delta\Phi_{ul} \sim 45^o$, which is different from the minimum observed for the plasma boundary displacement at the midplane. No clear dependence with $\Delta\Phi_{ul}$ is observed for the $n = 4, 6, 8$ components. It is also noted that the functional form of the fast-ion orbit displacement curve seems to be different from the plasma boundary displacement curve shown in Fig.4 (b).

In order to infer the fast-ion orbit displacement induced by MPs, we apply the formula shown in Eq.2, where we now consider the correction due to the 3D plasma boundary displacement. It is important to notice that the correction due to the plasma boundary displacement needs to be taken at the probe beam birth position. This is the volume where the NBI injection geometry intersects the separatrix ϕ_{NBI}. Therefore, we need to take into account the toroidal and the poloidal shifts between the Li-BES measurement position and the probe beam birth position. This is illustrated in Fig.7 (a), where the modulation in the FILD signal is plotted in blue, the modulation of the plasma boundary measured at the Li-BES positions is plotted in magenta, and in red at the position of the intersection between NBI Q8 and the separatrix. The resulting fast-ion orbit displacement is plotted in green. This analysis is done using the fits to the FILD and the Li-BES signals that

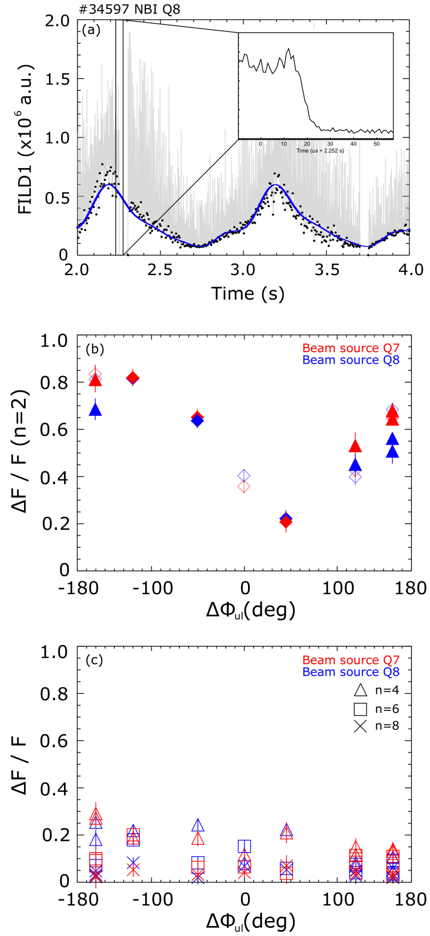

Figure 6. (a) Time evolution of FILD1 signal in AUG shot 34597. In grey the raw FILD signal. In black, the experimental datapoints after filtering the ELMs. In blue, the fit to the experimental datapoints. The inlet figures illustrates the decay time of the raw FILD signal during a beam notch. (b) Measured n=2 component of the FILD modulation as a function of $\Delta\Phi_{ul}$. The empty symbols correspond to the cases with the wrong coil polarity, described in Table 1. (c) Same as (b) but for the n=4,6,8 components.

have been discussed previously.

Fig.7 shows the resulting n=2 component of the MP induced fast-ion orbit displacement for both probe beams as a function of $\Delta\Phi_{ul}$. The transparent symbols represent the "apparent" kick, i.e. using Eq.1, while the full symbols represent the real kick, i.e. using Eq.2, so taking into account the correction due to 3D plasma boundary displacement. For reference, the shaded area represents the maximum possible correction to the "apparent" kick due to the 3D plasma boundary displacement for the NBI Q7 case, i.e. $\xi^{apparent} = L_{n_e} \cdot \frac{\Delta F}{\langle F \rangle} \pm \xi^{pl}$, for the n=2 component. It can be seen that this correction does not change qualitatively the results.

Again, no difference is observed between probe beams Q7 and Q8, within the experimental error bars.

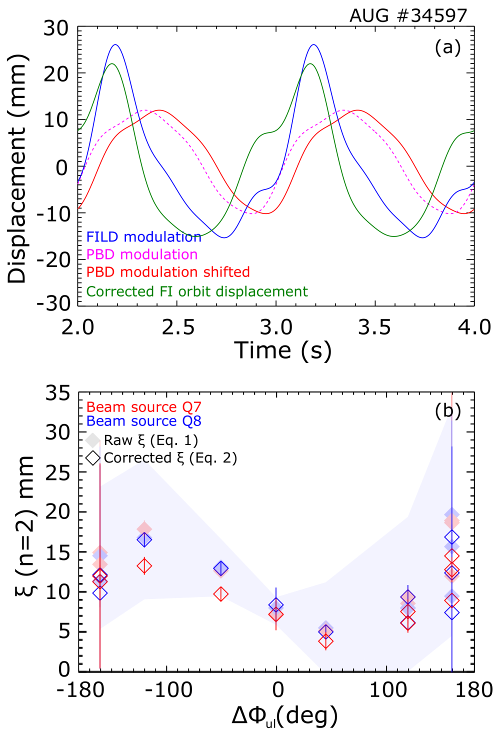

Figure 7. (a) Time evolution of the PBD, FILD signal, and the resulting PBD corrected fast-ion orbit displacement (using Eq.2). (b) MP induced fast-ion orbit displacement as a function of $\Delta\Phi_{ul}$. The transparent symbols represent the apparent kick (Eq.1), while the full symbols represent the corrected kick (Eq.2).

The fast-ion orbit displacement ranges between 3 and 20 mm approximately. The minimum of the fast-ion orbit displacement sits at $\Delta\Phi \sim 50^o$. Therefore, there is a clear shift of $\sim 50^o$ with respect to the plasma boundary displacement measured at the midplane, as shown in Fig.4. In these shots only ELM mitigation was achieved. However, it has been shown that in AUG the access to ELM suppression happens in a limited range of $\Delta\Phi_{ul}$ [10]. Therefore, this result suggests that, under certain circumstances, the MP induced fast-ion transport could be decoupled from ELM control. A more detailed discussion will follow in Section 5. In addition, it furthers supports the idea that the modulation of the FILD signal is not dominated by the 3D plasma boundary displacement.

4. Comparison to full orbit following simulations

These results have been compared to simulations performed with the orbit following code ASCOT [47]. Since in our experimental measurements we have extracted the orbit displacement taking into account the 3D plasma boundary displacement, in these simulations we can focus on measuring the orbit displacements induced by the MPs. The simulation setup is the following:

(i) Magnetic configuration: we consider both, the vacuum fields only and including the plasma response, as calculated by the MARS-F code [48, 49]. In both cases we consider only the n=2 and n=6 toroidal components of the fields.

(ii) Radial electric field: we include a radial electric field E_r, since it can have an impact on the fast-ion orbits [35]. However, we note that we have considered the same E_r for all simulations, independent from $\Delta\Phi_{ul}$. The limitations of this assumption will be discussed later. The E_r used in these simulations correspond to the typical for H-mode plasmas in AUG [50], with the minimum of the well at approximately $-40\ kV/m$.

(iii) The fast-ion markers are followed in full-orbit mode. We consider deuterium ions.

(iv) Markers: we fix the markers energy to 93 keV, which is the main NBI injection energy. We fix the initial R,Z position to that of the FILD probe position. At this position, we fix the pitch angle to the values corresponding to the probe beams Q7 ($\lambda = 0.63$) and Q8 ($\lambda = 0.41$). In reality, the NBI leads to a distribution of ions in R,Z and λ which are then lost to the FILD detector. The values that we select for these simulations correspond approximately to the centroid of such distribution. Then we start a set of 360 markers distributed along the full toroidal range $\phi = [0, 2\pi]$, in order to mimic the toroidal rigid rotation of the applied MPs, as in the experiment.

(v) We do not consider the wall of the machine.

The markers are then followed backwards in time for $\Delta t \sim 50\mu s$, which corresponds to a couple of poloidal bounces and is consistent with the experimental decay time measured at the FILD detector. Following this scheme, we are effectively mimicking an MP rigid rotation in a single simulation, and therefore it yields directly the orbit displacement we are searching for. For each marker, we measure the difference in their radial position after it completes a poloidal transit. This measurement is done at the maximum R along the particle orbit, regardless of it being at the midplane or somewhere else. Since we are following the markers in full-orbit mode, we measure the radial position of the marker at the low field side always at the same gyrophase angle.

An example is illustrated in Fig.8 where (a) shows the experimental FILD signal and (b) the results of the ASCOT simulations . This case corresponds to a set of markers with $\lambda = 0.40$ and started at $R_{ini} = 2.175$. The magnetic configuration is that of $\Delta\Phi = 120^o$ calculated including the plasma response.

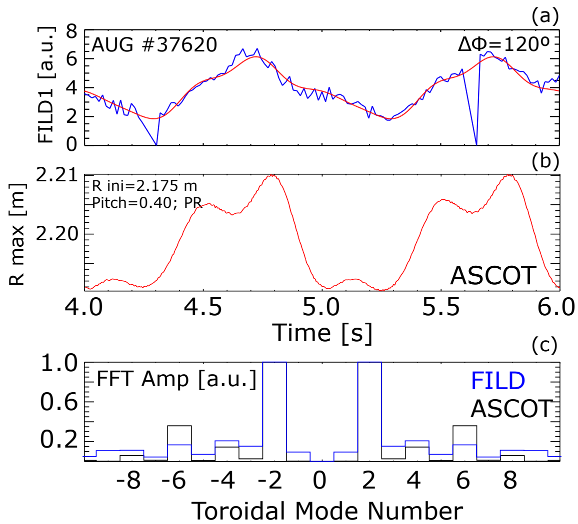

Figure 8. (a) Signal of FILD1 in shot AUG 37620, corresponding to a $\Delta\Phi = 120^o$. The ELM filtered signal is plotted in blue, while the fit is plotted in red. (b) Maximum radial position of the markers as a function of time. (c) Fourier spectrum of the resulting modulation.

It can be seen that a very smooth modulation is obtained, similar to that observed in the experiments. Here ϕ_{ini} was mapped into time by taking into account the rotation frequency of the MPs in the experiment. Furthermore, Fig.8(c) shows that, as in the experiment, that not only the dominant n=2 component shows up, but also the additional n=4 and n=6 components are observed.

We can repeat the same process for different MP spectra to build a curve representing the MP induced fast-ion orbit displacement vs $\Delta\Phi_{ul}$, which can be directly compared to the experimental results shown in Fig. 7.

This is shown in Fig.9, for markers started with a pitch angle $\lambda = 0.41$, which correspond to those of probe beam Q8 in the experiment. A radial scan is performed in the initial radial position R_{ini}, illustrated by different colors. Figure (a) shows the results using the vacuum approach while (b) shows the results including the plasma response. The dashed lines represent the total orbit displacement, while the full lines represent the extracted n=2 component. From Fig.9(a) we can make the following observations: first, that there is a smooth transition from outer to inner initial radial positions. The shape of the curve is kept the same, with the maximum of the orbit displacement at $\Delta\Phi_{ul} \sim 50^o$ and the minimum at $\Delta\Phi_{ul} \sim 180^o$. It can be seen that the largest orbit displacements are obtained at the outermost initial radial position of the markers, which seems reasonable due to the fact these orbits are closer to the MP coils, and therefore they explore regions with larger MP fields. The orbit displacement ranges from 5 to 15 mm. On the other hand, it can be seen that the difference between the total and the n=2 extracted component of the orbit displacement is small, indicating that the orbit displacement in this case is indeed dominated by the n=2 component of the perturbed field. If we now focus on the results including the plasma response, shown in Fig.9(b), we can see a similar behaviour. However, in this case, the position of the maximum and the minimum of the orbit displacement is slightly shifted with respect to the vacuum case. This shift becomes more clear for simulations with different pitch angles. This is illustrated as an example in Fig.9 (c) and (d), which correspond to a pitch angle of $\lambda = 0.48$. This suggests that, as already acknowledged in previous works [16, 33], the plasma response needs to be included in orbit following simulations in order to have accurate predictions. However, if we compare the results of these simulations with the experimental measurements, we observe a shift of the curve of $\sim 180^o$.

The same set of simulations is done but for markers with $\lambda = 0.63$, which correspond to those of probe beam Q7 in the experiment. The results are shown in Fig.10, following a similar scheme. We first discuss the simulations in vacuum approach, shown in Fig.10(a). In this case, we observe that the shape of the curve changes considerably when performing the radial scan. It can be seen how the minimum and maximum values of the orbit displacement are shifted towards different values. Additional simulations for slightly different values of the pitch angle and initial radial location show that the shift in the minimum does not follow a clear trend. In this case the orbit displacements range between 2 and 15 mm. Furthermore, it can also be seen that the difference between the total orbit displacement and the n=2 component is larger than in the case of trapped particles, suggesting that in these cases, although the n=2 component is still dominant, other components need to be considered as well.

If we now focus on the simulations including the plasma response, shown in Fig.10 (b) we see that the shape of the curve does not change qualitatively. Only small differences in the measured orbit displacement can be observed. However, again, the difference between vacuum and plasma response simulations is found to depend on the particle's pitch angle. This is illustrated in Fig.10 (c), where the orbit displacement calculated in vacuum and plasma response are compared for a test-ion marker with pitch angle $\lambda = 0.57$. Here the impact of the plasma response is larger for the cases with larger R_{ini}, where the difference with respect to the vacuum simulations becomes more clear. The Poincare plot of the magnetic field lines is shown in Fig.11, for the vacuum approach case in

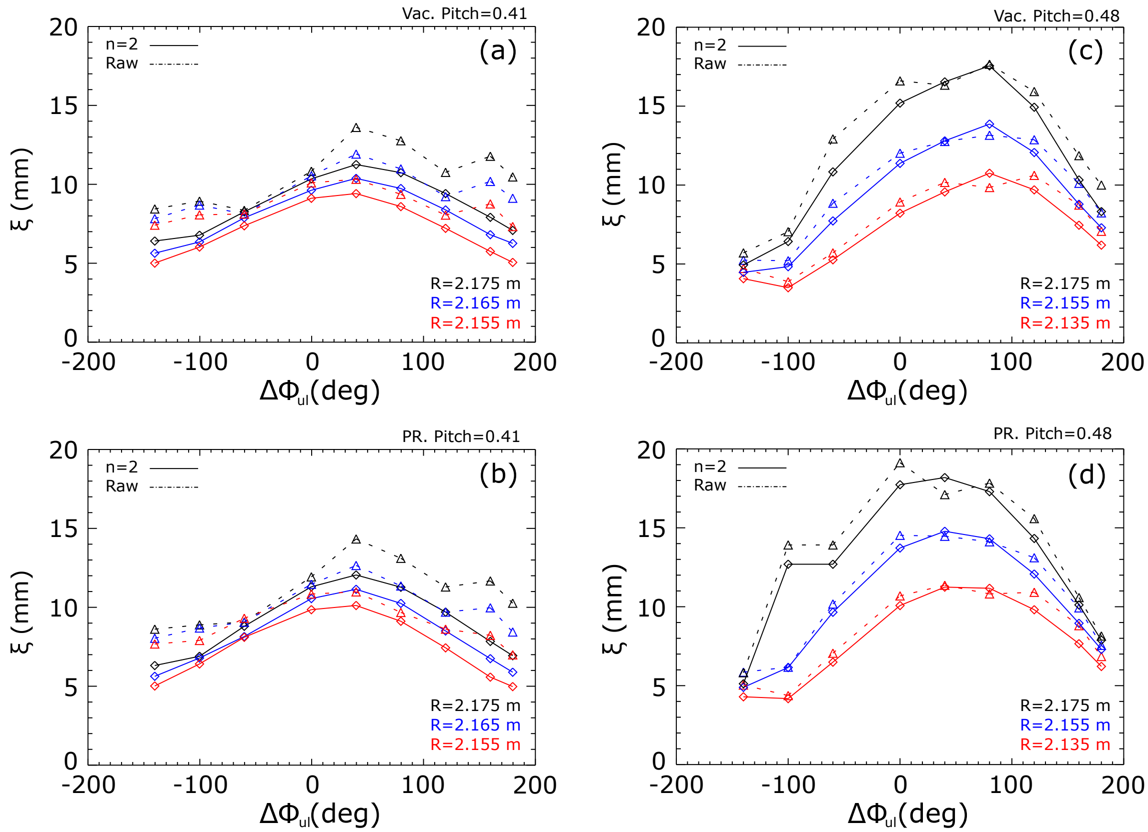

Figure 9. ASCOT simulations of the fast-ion first orbit displacement as a function of $\Delta\Phi_{ul}$, for deuterium ions with pitch angle $\lambda = 0.41$ and $\lambda = 0.48$, corresponding to trapped particles. The dashed lines represent the total orbit displacement, while the full lines represent the extracted n=2 component. (a) and (c) show the simulations carried out using the vacuum fields including only the n=2 and n=6 components for $\lambda = 0.41$ and $\lambda = 0.48$ respectively. (b) and (d) show the simulations carried out including the plasma response as calculated by MARS-F, including only the n=2 and n=6 components for $\lambda = 0.41$ and $\lambda = 0.48$ respectively. In all cases, the different colors indicate a different initial radial position.

(a) and for the plasma response case in (b). Here no clear shielding of the stochastic layer is observed at the edge of the plasma, suggesting that the differences in the orbit displacement between the vacuum and plasma response case might come from changes in the resonant interaction between the perturbed fields and the particle, rather than being induced by the magnetic field stochasticity. In (c) and (d), the corresponding Poincare plots of fast-ion markers with $E = 93$ keV and $\lambda = 0.63$ are shown.

However, again, a clear match with the experimental measurements is not obtained. In the following, we speculate about several reasons that could explain the disagreement between these ASCOT simulations and the experimental measurements. The first one is related to the E_r used in the simulations. Our simulations have been done using the same E_r for all cases, i.e. all $\Delta\Phi_{ul}$. However, in AUG it has been shown that the E_r can be affected by the applied MP spectrum, in particular the depth of the E_r well, in L-mode plasmas [51] and at the L-H transition [52]. Therefore, a dependence of E_r with the applied MP phasing could also be expected in H-mode plasmas. On the other hand, it has also been shown that the E_r has an impact on the fast-ion orbits- mainly by modifying the toroidal precession frequency [35] - which in turn can affect the orbital resonances [16]. Therefore, including the E_r in the simulations consistently with the $\Delta\Phi_{ul}$ might be needed. Another possible reason could be related to the plasma response model. In our simulations we have used the plasma response calculated with the MARS-F code, which implements a single fluid resistive linear MHD model. In these simulations the plasma flow was considered to be the mass flow. However, simulations with MARS-F have shown that the plasma response fields can change considerably when considering different plasma flow models [53] as e.g. the electron diamagnetic flow [48]. In addition, other plasma response models could be investigated, such as the one implemented in MEGA [54, 55], a resistive, non-linear hybrid kinetic-MHD code which would account for the impact of fast-ion kinetic effects on the plasma response. Finally, a possible shadowing effect of the 3D wall on the FILD detector should be investigated. In reality, the wall of the AUG tokamak is 3D, with many toroidally and poloidally localized structures that could eventually be blocking some of the particles trajectories that otherwise would reach the detector. Preliminary simulations suggest that this effect is not important, but a more in depth analysis is needed. Evaluating the quantitative impact of all these hypothesis requires a major effort, mainly from the modelling side, which we consider is out of the scope of this paper.

5. Conclusions

The impact of externally applied MPs on fast-ion confinement has been investigated by means of the LIBP technique in the ASDEX Upgrade tokamak. The LIBP technique provides an experimental measurement of MP induced fast-ion orbit displacement by probing first orbit losses from NBI systems. These measurements can be directly compared to simulation results, which allow us to validate state-of-the-art codes and give us confidence on predictions towards future machines, such as ITER.

In AUG, a set of experiments were carried out where the orbit displacement of two different fast-ion populations - associated to two different NBI sources, Q7 and Q8, generating passing and trapped orbit populations respectively - has been measured as a function of the applied MP spectrum, controlled by $\Delta\Phi_{ul}$. The impact of 3D density modulation on the FILD signal has been investigated. ASCOT modelling, in a fixed 3D magnetic configuration, but taking into account radial shifts of the kinetic profiles of $\pm 1cm$, as measured in the experiment, suggest that a modulation of up to 50% of the FILD signal is possible. Therefore, a generalization of the LIBP technique has been derived for its application to MP experiments. The measured fast-ion orbit displacements include a correction which accounts for the impact of 3D density profile modulation on the FILD signal. It is found that, within errorbars, no difference can be found between the two fast-ion populations probed. The measured fast-ion orbit displacement ranges from 3 to 20 mm approximately. It is found that the minimum for the fast-ion orbit displacement sits at $\Delta\Phi_{ul} \sim 50^o$, while the minimum of the plasma boundary displacement sits at $\Delta\Phi_{ul} \sim 0^o$.

These experiments were carried out in ELM mitigated H-mode plasmas. A similar experimental study targeting ELM suppressed plasmas is to be carried out in the near future. Future work will also focus on the dependence of fast-ion losses with the amplitude of the applied MP and its relation to the onset of ELM mitigation and suppression. Several experiments have been carried out in AUG in this respect and they will be the subject of a future publication.

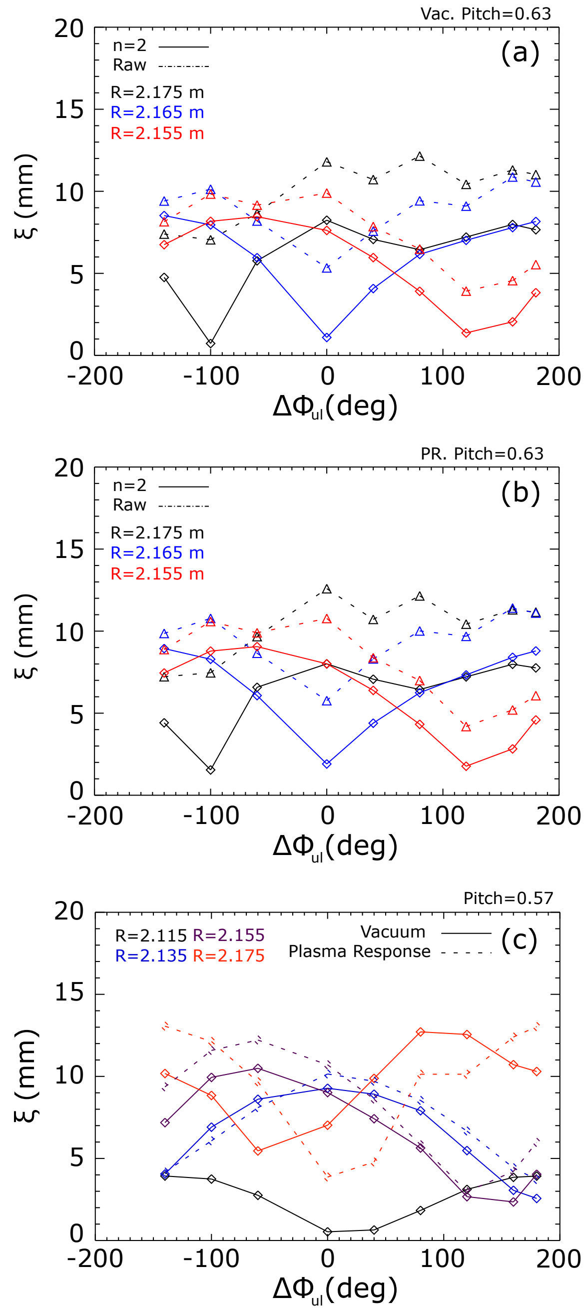

Figure 10. ASCOT simulations of the fast-ion first orbit displacement as a function of $\Delta\Phi_{ul}$, for deuterium ions with pitch angle $\lambda = 0.63$, corresponding to passing particles. The dashed lines represent the total orbit displacement, while the full lines represent the extracted n=2 component. (a) Simulations carried out using the vacuum fields including only the n=2 and n=6 components. (b) Simulations carried out including the plasma response as calculated by MARS-F, including only the n=2 and n=6 components. In both cases, the different colors indicate a different initial radial position. (c) Simulations for deuterium ions with $\lambda = 0.57$. Different colors correspond to different initial radial position. Full lines correspond to simulations in vacuum, while dashed lines include the plasma response.

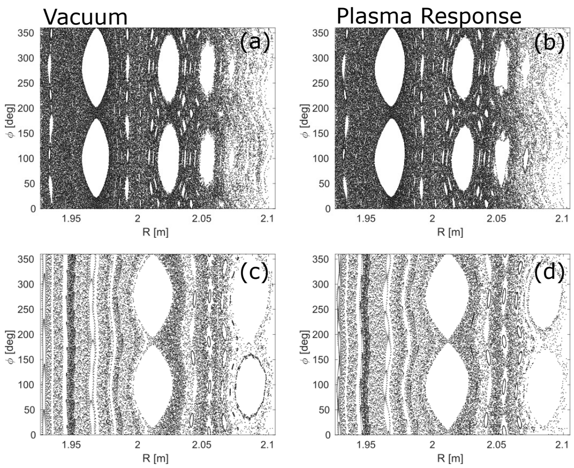

Figure 11. Poincare plot of (a) magnetic field lines in vacuum approach, (b) magnetic field lines including the plasma response, and fast-ion marker with $E = 93$ keV and $\lambda = 0.63$ in vacuum (c) and including plasma response (d). All cases correspond to a $\Delta\Phi_{ul} = 40^o$

As stated above, the main goal of this work is to provide experimental measurements that can serve as a testbed to validate state-of-the-art codes and to improve our confidence in the predictions towards future machines. A first attempt has been presented here by performing simulations with the ASCOT code, both in vacuum approach and including the plasma response as calculated by the MARS-F code. The simulations capture some of the experimental features. First, it is observed that in addition to the dominant n=2 toroidal component of the perturbation, additional sidebands such as the n=4 and n=6 component might be important under certain circumstances, as observed in the experiment. Second, the magnitude of the first-orbit fast-ion orbit displacement ranges between 2 and 15 mm, which is of the same order of the one measured experimentally. However, these simulations do not perfectly match the dependence of the fast-ion orbit displacement with the applied MP spectrum $\Delta\Phi_{ul}$. We speculate about possible reasons to explain this missmatch. First, the variation of the radial electric field - mainly the depth of the E_r well - with the applied $\Delta\Phi_{ul}$ should be taken into account consistently in the simulations. Second, the dependence of the fast-ion transport with the plasma response model should also be investigated. And finally, a possible shadowing effect due to the realistic 3D wall structure of the vessel should also be investigated. The testing of these hypothesis would require a major effort from the modelling side, which we consider is out of the scope of this paper. Therefore, we leave this for future work. It should also be noted that in this work the effect of the toroidal field ripple has been ignored. While this approach seems valid for AUG given the relatively small ripple, this needs to be considered when making predictions towards future devices such as ITER, as well as the presence of test blanket modules [25]

Nevertheless, these simulations also provide valuable insights of the mechanisms involved in the MP induced fast-ion transport. The radial scans show that, for trapped particles, the dependence of ξ^{FI} with $\Delta\Phi_{ul}$ is barely altered -only the amplitude of the kick is affected-, while for passing particles this dependence is strongly altered. This seems to be consistent with the geometrical resonances picture illustrated in Fig.4 from [16], suggesting that the first-orbit fast-ion losses are indeed dominated by the edge resonant transport layer mechanism. For the trapped particles, it can be seen that the resonant structures extend towards the scrape-off layer and are aligned along the radial direction. However, we find the opposite situation for the passing particles: the resonant structures are aligned along the pitch angle direction, and moving radially implies changing from one resonance to another. Furthermore, these structures become less clear towards the scrape-off layer, suggesting that the stochasticity of the magnetic field lines might become important in that region of phase-space. In addition, it is shown that including the plasma response has an effect on the fast-ion orbit displacement, which reinforces the idea, already raised in previous works [29, 16, 28, 36], that the plasma response needs to be included to properly model fast-ion transport induced by MPs. While ELM control is usually linked to the plasma boundary displacement at the X-point [56], the difference in the experimental measurement of the plasma boundary displacement at the midplane and the fast-ion orbit displacement, together with the modelling results which show a velocity-space dependence of the orbit displacement with $\Delta\Phi_{ul}$, suggest that beam-ion confinement could be decoupled from ELM control.

Finally some considerations on the applicability of this work and its limitations are discussed. In this work it has been experimentally shown that the MP induced fast-ion first-orbit displacement is a function of the applied spectrum via $\Delta\Phi_{ul}$. For a fixed scenario, a minimum in the MP induced kick can be found for specific fast-ion populations. Then, two different optimization strategies can be thought of. First, the "toroidal phase optimization", which consists in applying the MP fields with a relative toroidal phase with respect to the target fast-ion population, such that the latter sits in a region of $\delta P_\phi > 0$, where $P_\phi = mRv_\phi - Ze\Psi$ is the particle toroidal canonical angular momentum. This was the approach followed in [28], and it relies on a static MP configuration. However, it might be possible that, for future machines such as ITER, the application of dynamic MP configurations, such as e.g. rigidly rotating MPs at fixed $\Delta\Phi_{ul}$, are needed in order to redistribute heat loads both in the divertor plates [57, 58, 59], or in the first wall [22]. In such a case, the toroidal phase optimization might not be enough. Instead, searching for the MP spectral configuration ($\Delta\Phi_{ul}^{opt}$) which minimizes the target fast-ion orbit displacement, might be an option. Here, $\Delta\Phi_{ul}^{opt}$ should be inside the window compatible with appropriate ELM control.

The modelling results suggest that the mechanism dominating first-orbit fast-ion losses are the linear and non-linear resonances between the MP fields and the fast-ion orbits. This means that this is a highly phase-space dependent mechanism. Therefore, the applicability of the above discussed optimization methods is limited to highly anisotropic fast-ion distribution functions. For a fixed scenario and MP configuration, there are fast-ion phase-space regions compatible with an improved first-orbit confinement alternating with regions with a degraded first-orbit confinement. If the actual fast-ion distribution is highly anisotropic, one could eventually taylor it such that it matches with these *improved* phase-space regions. This is the case for NBI birth distribution functions which have been studied so far. These are, indeed, highly anisotropic: $f = f(E, \lambda, \vec{r}) \propto \delta(E - E_{inj}) \cdot \delta(\lambda - \lambda_{inj}) \cdot \delta(\vec{r} - \vec{r_{inj}})$. Therefore, the optimization methods discussed above can be applied, which is of interest since the power carried by NBI first-orbit losses might be non-negligible under certain circumstances [23, 25].

However the picture changes when we consider *less* anisotropic distribution functions. Then the fast-ion distribution function will fill, unavoidably, phase-space regions with *improved* and *degraded* first-orbit fast-ion confinement. This could be the case of fast-ion distribution functions of other nature such as, e.g. slowed down NBI distribution functions, or ultimately, fusion born alpha particle distribution functions. In these cases other loss mechanisms might become important and the optimization procedure discussed above might not apply.

Acknowledgments

This work has been carried out within the framework of the EUROfusion Consortium, funded by the European Union via the Euratom Research and Training Programme (Grant Agreement No 101052200 — EUROfusion). Views and opinions expressed are however those of the author(s) only and do not necessarily reflect those of the European Union or the European Commission. Neither the European Union nor the European Commission can be held responsible for them. This research was supported in part by the Spanish Ministry of Science and Innovation under grant no. FJC2019-041092-I, the Helmholtz Association under grant no. VH-NG-1350, and DOE under grant no. DE-SC0020337.

References

[1] F. Wagner, G. Becker, K. Behringer, D. Campbell, A. Eberhagen, W. Engelhardt, G. Fussmann, O. Gehre, J. Gernhardt, G. v. Gierke, G. Haas, M. Huang, F. Karger, M. Keilhacker, O. Klueber, M. Kornherr, K. Lackner, G. Lisitano, G. G. Lister, H. M. Mayer, D. Meisel, E. R. Mueller, H. Murmann, H. Niedermeyer, W. Poschenrieder, H. Rapp, H. Roehr, F. Schneider, G. Siller, E. Speth, A. Staebler, K. H. Steuer, G. Venus, O. Vollmer, and Z. Yu. Regime of improved confinement and high beta in neutral-beam-heated divertor discharges of the ASDEX tokamak. *Physical Review Letters*, 49(19):1408–1412, nov 1982.

[2] H Zohm. Edge localized modes (ELMs). *Plasma Physics and Controlled Fusion*, 38(2):105–128, feb 1996.

[3] J. W. Connor, A. Kirk, H. R. Wilson, and Sadruddin Benkadda. Edge Localised Modes (ELMs): Experiments and Theory. In *AIP Conference Proceedings*, volume 1013, pages 174–190. AIP, may 2008.

[4] P. B. Snyder, H. R. Wilson, and X. Q. Xu. Progress in the peeling-ballooning model of edge localized modes: Numerical studies of nonlinear dynamics. In *Physics of Plasmas*, volume 12, pages 1–7. American Institute of Physics, may 2005.

[5] T. Eich, A. W. Leonard, R. A. Pitts, W. Fundamenski, R. J. Goldston, T. K. Gray, A. Herrmann, A. Kirk, A. Kallenbach, O. Kardaun, A. S. Kukushkin, B. Labombard, R. Maingi, M. A. Makowski, A. Scarabosio, B. Sieglin, J. Terry, and A. Thornton. Scaling of the tokamak near the scrape-off layer H-mode power width and implications for ITER. *Nuclear Fusion*, 53(9):093031, sep 2013.

[6] T. Eich, B. Sieglin, A. J. Thornton, M. Faitsch, A. Kirk, A. Herrmann, and W. Suttrop. ELM divertor peak energy fluence scaling to ITER with data from JET, MAST and ASDEX upgrade. *Nuclear Materials and Energy*, 12:84–90, aug 2017.

[7] B Sieglin, M Faitsch, T Eich, A Herrmann, W Suttrop, JET Collaborators, the MST1 Team, and the ASDEX Upgrade Team. Progress in extrapolating divertor heat fluxes towards large fusion devices. *Physica Scripta*, T170(T170):014071, dec 2017.

[8] R.P. Wenninger, M. Bernert, T. Eich, E. Fable, G. Federici, A. Kallenbach, A. Loarte, C. Lowry, D. McDonald, R. Neu, T. Pütterich, P. Schneider, B. Sieglin, G. Strohmayer, F. Reimold, and M. Wischmeier. DEMO divertor limitations during and in between ELMs. *Nuclear Fusion*, 54(11):114003, nov 2014.

[9] Q M Hu, R Nazikian, N C Logan, J.-K Park, C Paz-Soldan, S M Yang, B A Grierson, Y In, Y M Jeon, M Kim, S K Kim, D M Orlov, G Y Park, Q Yu, and) R Nazikian. Predicting operational windows of ELMs suppression by resonant magnetic perturbations in the DIII-D and KSTAR tokamaks. *Phys. Plasmas*, 28:52505, 2021.

[10] W. Suttrop, A. Kirk, V. Bobkov, M. Cavedon, M. Dunne, R. M. McDermott, H. Meyer, R. Nazikian, C. Paz-Soldan, D. A. Ryan, E. Viezzer, and M. Willensdorfer. Experimental conditions to suppress edge localised modes by magnetic perturbations in the ASDEX

Upgrade tokamak. *Nuclear Fusion*, 58(9):096031, sep 2018.

[11] Todd E. Evans, Richard A. Moyer, Keith H. Burrell, Max E. Fenstermacher, Ilon Joseph, Anthony W. Leonard, Thomas H. Osborne, Gary D. Porter, Michael J. Schaffer, Philip B. Snyder, Paul R. Thomas, Jonathan G. Watkins, and William P. West. Edge stability and transport control with resonant magnetic perturbations in collisionless tokamak plasmas. *Nature Physics*, 2(6):419–423, jun 2006.

[12] Jong Kyu Park, Young Mu Jeon, Yongkyoon In, Joon Wook Ahn, Raffi Nazikian, Gunyoung Park, Jaehyun Kim, Hyung Ho Lee, Won Ha Ko, Hyun Seok Kim, Nikolas C. Logan, Zhirui Wang, Eliot A. Feibush, Jonathan E. Menard, and Michael C. Zarnstroff. 3D field phase-space control in tokamak plasmas. *Nature Physics*, 14(12):1223–1228, dec 2018.

[13] Y. Sun, Y. Liang, Y. Q. Liu, S. Gu, X. Yang, W. Guo, T. Shi, M. Jia, L. Wang, B. Lyu, C. Zhou, A. Liu, Q. Zang, H. Liu, N. Chu, H. H. Wang, T. Zhang, J. Qian, L. Xu, K. He, D. Chen, B. Shen, X. Gong, X. Ji, S. Wang, M. Qi, Y. Song, Q. Yuan, Z. Sheng, G. Gao, P. Fu, and B. Wan. Nonlinear Transition from Mitigation to Suppression of the Edge Localized Mode with Resonant Magnetic Perturbations in the EAST Tokamak. *Physical Review Letters*, 117(11):115001, sep 2016.

[14] M Garcia-Munoz, S Äkäslompolo, P. De Marne, M G Dunne, R Dux, T E Evans, N M Ferraro, S Fietz, C Fuchs, B Geiger, A Herrmann, M Hoelzl, B Kurzan, N Lazanyi, R M McDermott, M Nocente, D C Pace, M Rodriguez-Ramos, K Shinohara, E Strumberger, W Suttrop, M A Van Zeeland, E Viezzer, M Willensdorfer, and E Wolfrum. Fast-ion losses induced by ELMs and externally applied magnetic perturbations in the ASDEX Upgrade tokamak. *Plasma Physics and Controlled Fusion*, 55(12):124014, dec 2013.

[15] M. Garcia-Munoz, S. Äkäslompolo, O. Asunta, J. Boom, X. Chen, I. G.J. Classen, R. Dux, T. E. Evans, S. Fietz, R. K. Fisher, C. Fuchs, B. Geiger, M. Hoelzl, V. Igochine, Y. M. Jeon, J.Y. Kim, J. Y. Kim, B. Kurzan, N. Lazanyi, T. Lunt, R. M. McDermott, M. Nocente, D. C. Pace, T. L. Rhodes, M. Rodriguez-Ramos, K. Shinohara, W. Suttrop, M. A. Van Zeeland, E. Viezzer, M. Willensdorfer, and E. Wolfrum. Fast-ion redistribution and loss due to edge perturbations in the ASDEX Upgrade, DIII-D and KSTAR tokamaks. *Nuclear Fusion*, 53(12):123008, dec 2013.

[16] L Sanchis, M Garcia-Munoz, A Snicker, D A Ryan, D Zarzoso, L Chen, J Galdon-Quiroga, M Nocente, J F Rivero-Rodriguez, M Rodriguez-Ramos, W Suttrop, M A Van Zeeland, E Viezzer, M Willensdorfer, F Zonca, and the ASDEX Upgrade Team and the EUROfusion MST1 Team. Characterisation of the fast-ion edge resonant transport layer induced by 3D perturbative fields in the ASDEX Upgrade tokamak through full orbit simulations. *Plasma Physics and Controlled Fusion*, 61(1):014038, jan 2019.

[17] M A Van Zeeland, N M Ferraro, W W Heidbrink, G J Kramer, D C Pace, X Chen, T E Evans, R K Fisher, M García-Muñoz, J M Hanson, M J Lanctot, L L Lao, R A Moyer, R Nazikian, and D M Orlov. Modulation of prompt fast-ion loss by applied n = 2 fields in the DIII-D tokamak. *Plasma Physics and Controlled Fusion*, 56(1):015009, jan 2014.

[18] M.A. Van Zeeland, N.M. Ferraro, B.A. Grierson, W.W. Heidbrink, G.J. Kramer, C.J. Lasnier, D.C. Pace, S.L. Allen, X. Chen, T.E. Evans, M. García-Muñoz, J.M. Hanson, M.J. Lanctot, L.L. Lao, W.H. Meyer, R.A. Moyer, R. Nazikian, D.M. Orlov, C. Paz-Soldan, and A. Wingen. Fast ion transport during applied 3D magnetic perturbations on DIII-D. *Nuclear Fusion*, 55(7):073028, jul 2015.

[19] Kimin Kim, Hogun Jhang, Junghee Kim, and T. Rhee. Enhanced fast ion prompt loss due to resonant magnetic perturbations in KSTAR. *Physics of Plasmas*, 25(12):122511, dec 2018.

[20] K G Mcclements, R J Akers, W U Boeglin, M Cecconello, D Keeling, O M Jones, A Kirk, I Klimek, R V Perez, K Shinohara, and K Tani. The effects of resonant magnetic perturbations on fast ion confinement in the mega amp spherical tokamak. *Plasma Physics and Controlled Fusion*, 60(9):095005, sep 2015.

[21] K. G. McClements, K. Tani, R. J. Akers, Y. Q. Liu, K. Shinohara, H. Tsutsui, and S. Tsuji-Iio. The effects of resonant magnetic perturbations and charge-exchange reactions on fast ion confinement and neutron emission in the Mega Amp Spherical Tokamak. *Plasma Physics and Controlled Fusion*, 60(9):095005, jul 2018.

[22] K. Tani, K. Shinohara, T. Oikawa, H. Tsutsui, S. Miyamoto, Y. Kusama, and T. Sugie. Effects of ELM mitigation coils on energetic particle confinement in ITER steady-state operation. *Nuclear Fusion*, 52(1):013012, jan 2012.

[23] K. Shinohara, K. Tani, T. Oikawa, S. Putvinski, M. Schaffer, and A. Loarte. Effects of rippled fields due to ferritic inserts and ELM mitigation coils on energetic ion losses in a 15MA inductive scenario in ITER. *Nuclear Fusion*, 52(9):094008, sep 2012.

[24] T Koskela, O Asunta, E Hirvijoki, T Kurki-Suonio, and S Äkäslompolo. ITER edge-localized modes control coils: the effect on fast ion losses and edge confinement properties. *Plasma Physics and Controlled Fusion*, 54(10):105008, oct 2012.

[25] T. Kurki-Suonio, S. Äkäslompolo, K. Särkimäki, J. Varje, O. Asunta, M. Cavinato, M. Gagliardi, E. Hirvijoki, V. Parail, G. Saibene, S. Sipilä, and A. Snicker. Effect of the European design of TBMs on ITER wall loads due to fast ions in the baseline (15 MA), hybrid (12.5 MA), steady-state (9 MA) and half-field (7.5 MA) scenarios. *Nuclear Fusion*, 56(11):112024, nov 2016.

[26] Jari Varje, Otto Asunta, Mario Cavinato, Mario Gagliardi, Eero Hirvijoki, Tuomas Koskela, Taina Kurki-Suonio, Yueqiang Liu, Vassili Parail, Gabriella Saibene, Seppo Sipilä, Antti Snicker, Konsta Särkimäki, and Simppa Äkäslompolo. Effect of plasma response on the fast ion losses due to ELM control coils in ITER. *Nuclear Fusion*, 56(4):046014, 2016.

[27] Konsta Sarkimaki, Jari Varje, Marina Bécoulet, Yueqiang Liu, and Taina Kurki-Suonio. Mechanics of ELM control coil induced fast particle transport in ITER. *Nuclear Fusion*, 58(7):076021, jun 2018.

[28] L. Sanchis, M. Garcia-Munoz, E. Viezzer, A. Loarte, L. Li, Y. Q. Liu, A. Snicker, L. Chen, F. Zonca, S. D. Pinches, and D. Zarzoso. Optimizing beam-ion confinement in ITER by adjusting the toroidal phase of the 3D magnetic fields applied for ELM control. *Nuclear Fusion*, 61(4):46006–46020, apr 2021.

[29] David Pfefferle, Cyril Misev, Wilfred A. Cooper, and Jonathan P. Graves. Impact of RMP magnetic field simulation models on fast ion losses. *Nuclear Fusion*, 55(1):012001, jan 2015.

[30] Kouji Shinohara, Yasuhiro Suzuki, Junghee Kim, Jun Young Kim, Young Mu Jeon, Andreas Bierwage, and Tongnyeol Rhee. Investigation of fast ion behavior using orbit following Monte-Carlo code in magnetic perturbed field in KSTAR. *Nuclear Fusion*, 56(11):112018, aug 2016.

[31] M. L. Mou, Z. T. Wang, N. Wu, S. Y. Chen, and C. J. Tang. Effect of resonant magnetic perturbations on fast ion prompt loss in tokamaks. *Nuclear Fusion*, 57(4):046023,

apr 2017.

[32] Yingfeng Xu, Wenfeng Guo, Lei Ye, Xiaotao Xiao, Shaojie Wang, and Siqiang Zhu. Loss and redistribution of energetic passing ions with resonant magnetic perturbations. *Physics of Plasmas*, 25(1):012502, jan 2018.

[33] K. He, B. N. Wan, Y. Sun, M. Jia, T. Shi, H. H. Wang, and X. J. Zhang. Resonant effects on the loss of energetic trapped ions induced by low-n resonant magnetic perturbations. *Nuclear Fusion*, 59(12):126026, dec 2019.

[34] Kaiyang He, Youwen Sun, B. N. Wan, Shuai Gu, and Manni Jia. Roles of primary and sideband resonances in the confinement of energetic passing ions under resonant magnetic perturbations. *Nuclear Fusion*, 60(12), sep 2020.

[35] Haotian Huang and Lu Wang. Effects of resonant magnetic perturbations on the loss of energetic ions in tokamak pedestal. *Plasma Science and Technology*, 22(10), jul 2020.

[36] K. He, Y. Sun, B. N. Wan, S. Gu, M. Jia, and Y. Hu. Full-orbit simulation of fast ion loss under resonant magnetic perturbations in the EAST tokamak. *Nuclear Fusion*, 61(1):016009, jan 2021.

[37] X. Chen, W.W. Heidbrink, G.J. Kramer, M.A. Van Zeeland, M.E. Austin, R.K. Fisher, R. Nazikian, D.C. Pace, and C.C. Petty. Prompt non-resonant neutral beam-ion loss induced by Alfvén eigenmodes in the DIII-D tokamak. *Nuclear Fusion*, 53(12):123019, dec 2013.

[38] Xi Chen, W. W. Heidbrink, M. A. Van Zeeland, G. J. Kramer, D. C. Pace, C. C. Petty, M. E. Austin, R. K. Fisher, J. M. Hanson, R. Nazikian, and L. Zeng. Using neutral beams as a light ion beam probe (invited). *Review of Scientific Instruments*, 85(11):11E701, nov 2014.

[39] Xi Chen, G. J. Kramer, W. W. Heidbrink, R. K. Fisher, D. C. Pace, C. C. Petty, M. Podesta, and M. A. Van Zeeland. Non-linear wave-particle interactions and fast ion loss induced by multiple Alfvén eigenmodes in the DIII-D tokamak. *Nuclear Fusion*, 54(8):083005, aug 2014.

[40] M. Garcia-Munoz, H. U. Fahrbach, and H. Zohm. Scintillator based detector for fast-ion losses induced by magnetohydrodynamic instabilities in the ASDEX upgrade tokamak. *Review of Scientific Instruments*, 80(5):053503, may 2009.

[41] J Galdon-Quiroga, M Garcia-Munoz, M Salewski, A S Jacobsen, L Sanchis-Sanchez, M Rodriguez-Ramos, J Ayllon-Guerola, J Garcia-Lopez, J Gonzalez-Martin, M C Jimenez-Ramos, J F Rivero-Rodriguez, E Viezzer, and the ASDEX Upgrade Team. Velocity-space sensitivity and tomography of scintillator-based fast-ion loss detectors. *Plasma Physics and Controlled Fusion*, 60(10):105005, oct 2018.

[42] M Willensdorfer, G Birkenmeier, R Fischer, F M Laggner, E Wolfrum, G Veres, F Aumayr, D Carralero, L Guimarãis, and B Kurzan. Characterization of the Li-BES at ASDEX Upgrade. *Plasma Physics and Controlled Fusion*, 56(2):025008, feb 2014.

[43] R Fischer, E Wolfrum, and J Schweinzer. Probabilistic lithium beam data analysis. *Plasma Physics and Controlled Fusion*, 50(8):085009, aug 2008.

[44] M Willensdorfer, S S Denk, E Strumberger, W Suttrop, B Vanovac, D Brida, M Cavedon, I Classen, M Dunne, S Fietz, R Fischer, A Kirk, F M Laggner, Y Q Liu, T Odstrčil, D A Ryan, E Viezzer, H Zohm, and I C Luhmann. Plasma response measurements of external magnetic perturbations using electron cyclotron emission and comparisons to 3D ideal MHD equilibrium. *Plasma Physics and Controlled Fusion*, 58(11):114004, nov 2016.

[45] H. J. Sun, E. Wolfrum, T. Eich, B. Kurzan, S. Potzel, and U. Stroth. Study of near scrape-off layer (SOL) temperature and density gradient lengths with Thomson scattering. *Plasma Physics and Controlled Fusion*, 57(12):125011, nov 2015.

[46] M. Willensdorfer, T. B. Cote, M. Griener, D. A. Ryan, E. Strumberger, W. Suttrop, N. Wang, M. Cavedon, S. S. Denk, M. Dunne, R. Fischer, J. Galdon-Quiroga, C. J. Ham, C. C. Hegna, M. Hoelzl, A. Kirk, M. Maraschek, F. Mink, N. Leuthold, F. Orain, E. P. Seliunin, and H. Zohm. Dynamics of ideal modes and subsequent ELM crashes in 3D tokamak geometry from external magnetic perturbations. *Plasma Physics and Controlled Fusion*, 61(1):014019, nov 2018.

[47] E. Hirvijoki, O. Asunta, T. Koskela, T. Kurki-Suonio, J. Miettunen, S. Sipilä, A. Snicker, and S. Äkäslompolo. ASCOT: Solving the kinetic equation of minority particle species in tokamak plasmas. *Computer Physics Communications*, 185(4):1310–1321, 2014.

[48] Yueqiang Liu, M. S. Chu, W. F. Guo, F. Villone, R. Albanese, G. Ambrosino, M. Baruzzo, T. Bolzonella, I. T. Chapman, A. M. Garofalo, C. G. Gimblett, R. J. Hastie, T. C. Hender, G. L. Jackson, R. J. La Haye, M. J. Lanctot, Y. In, G. Marchiori, M. Okabayashi, R. Paccagnella, M. Furno Palumbo, A. Pironti, H. Reimerdes, G. Rubinacci, A. Soppelsa, E. J. Strait, S. Ventre, and D. Yadykin. Resistive wall mode control code maturity: Progress and specific examples. *Plasma Physics and Controlled Fusion*, 52(10):104002, oct 2010.

[49] Yueqiang Liu, A. Kirk, and E. Nardon. Full toroidal plasma response to externally applied nonaxisymmetric magnetic fields. *Physics of Plasmas*, 17(12):122502, dec 2010.

[50] E. Viezzer, T. Pütterich, C. Angioni, A. Bergmann, R. Dux, E. Fable, R. M. McDermott, U. Stroth, and E. Wolfrum. Evidence for the neoclassical nature of the radial electric field in the edge transport barrier of ASDEX Upgrade. *Nuclear Fusion*, 54(1):012003, jan 2014.

[51] G. D. Conway, S. Fietz, H. W. Müller, T. Lunt, P. Simon, W. Suttrop, M. Maraschek, T. Happel, and E. Viezzer. Impact of magnetic perturbation coils on the edge radial electric field and turbulence in ASDEX Upgrade. *Plasma Physics and Controlled Fusion*, 57(1):014035, 2015.

[52] M. Willensdorfer, U. Plank, D. Brida, M. Cavedon, G. D. Conway, D. A. Ryan, W. Suttrop, R. Buchholz, M. Dunne, R. Fischer, M. Griener, J. Hobirk, S. Kasilov, A. Kirk, R. M. McDermott, T. Pütterich, G. Tardini, and Q. Yu. Dependence of the L–H power threshold on the alignment of external non-axisymmetric magnetic perturbations in ASDEX Upgrade. *Physics of Plasmas*, 29(3):032506, mar 2022.

[53] L. Li, Y. Q. Liu, G. L. Xia, Y. F. Wang, Q. B. Luan, W. D. Zhang, and F. C. Zhong. Screening of resonant magnetic perturbation fields assuming various plasma flow models. *Physics of Plasmas*, 28(8):082504, aug 2021.

[54] Y. Todo and T. Sato. Linear and nonlinear particle-magnetohydrodynamic simulations of the toroidal Alfvén eigenmode. *Physics of Plasmas*, 5(5 PART 1):1321–1327, apr 1998.

[55] J Gonzalez-Martin, M García-Muñoz, Y Todo, S E Sharapov, M Dunne, V Igochine, R Fischer, P Oyola, L Sanchis-Sanchez, A Jacobsen, Eleonora Viezzer, J Ayllon-Guerola, J Galdon-Quiroga, J Rivero-Rodriguez, J Dominguez-Palacios, M Rodríguez-Ramos, and J Dominguez-Abascal. Non-Linear 3D Hybrid Kinetic-MHD Simulations of Alfvén Eigenmodes in the ASDEX Upgrade Tokamak, 2018.

[56] A. Kirk, W. Suttrop, I. T. Chapman, Yueqiang Liu, R. Scannell, A. J. Thornton, L. Barrera Orte, P. Cahyna,

T. Eich, R. Fischer, C. Fuchs, C. Ham, J. R. Harrison, M. W. Jakubowski, B. Kurzan, S. Pamela, M. Peterka, D. Ryan, S. Saarelma, B. Sieglin, M. Valovic, and M. Willensdorfer. Effect of resonant magnetic perturbations on low collisionality discharges in MAST and a comparison with ASDEX Upgrade. *Nuclear Fusion*, 55(4):043011, mar 2015.

[57] The Asdex Upgrade Team, M. Faitsch, B. Sieglin, T. Eich, A. Herrmann, and W. Suttrop. Divertor heat load in ASDEX Upgrade L-mode in presence of external magnetic perturbation. *Plasma Physics and Controlled Fusion*, 59(9):095006, jul 2017.

[58] M. Faitsch, B. Sieglin, D. Brida, W. Suttrop, T. Lunt, T. Eich, and M. Wischmeier. Effect of magnetic perturbations for ELM control on divertor power loads, detachment and consequences of field penetration in ASDEX Upgrade. *Plasma Physics and Controlled Fusion*, 61(1):014008, jan 2019.

[59] A. Loarte, G. Huijsmans, S. Futatani, L. R. Baylor, T. E. Evans, D. M. Orlov, O. Schmitz, M. Becoulet, P. Cahyna, Y. Gribov, A. Kavin, A. Sashala Naik, D. J. Campbell, T. Casper, E. Daly, H. Frerichs, A. Kischner, R. Laengner, S. Lisgo, R. A. Pitts, G. Saibene, and A. Wingen. Progress on the application of ELM control schemes to ITER scenarios from the non-active phase to DT operation. *Nuclear Fusion*, 54(3):18, mar 2014.

Appendix A: Generalization of the LIBP formula for MP experiments

In this appendix Eq.2 is explicitly derived. The idea is illustrated in Fig.12. We begin by making the following assumption: the ion loss rate reaching the FILD detector is proportional to the birth profile fast-ion density, in our case associated to the NBI deposition.This assumption is reasonable for the case of first-orbit losses, as long as the fast-ions are energetic enough so that they can be considered collisionless in this timescale.

Then, the FILD signal modulation is twofold:

(i) Considering the MPs only: if the MP induced kick is larger, then we expect the lost ions reaching FILD to come from deeper in the plasma (blue circle). On the contrary, if the kick is smaller, or even in the opposite direction, then we would expect the lost ions to come from outer regions (red circles).

(ii) Considering the 3D PBD only: we now assume that the background 2D magnetic equilibrium remains unchanged. Therefore, the lost ions reaching the FILD would be always coming from the same radial location, indicated by the gray bar. If we now consider the effect of radially shifting the kinetic profiles (i.e. the fast-ion birth profile), the FILD signal would be modulated accordingly.

Therefore, we start by considering that:

$$F \propto n_b(\phi_b, R_b) \tag{5}$$

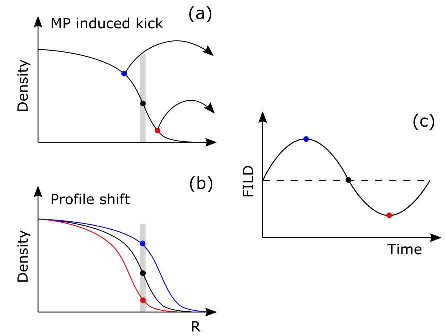

Figure 12. Cartoon illustration of how the FILD signal can be modulated by (a) MP induced fast-ion orbit displacements and (b) radial shifts in the kinetic profiles.(c) Both effects can lead to the same modulation of the FILD signal

where F is the FILD signal and n_b is the fast-ion birth density. The underscript b refers to the birth position of the ions reaching the FILD detector. Here n_b is a function of the radial coordinate (because we consider a realistic profile) and a function of the toroidal coordinate (because we consider the application of an external 3D perturbation).

Now we can expand n_b in the following form:

$$n_b(\phi, R) = n_b(R)|_{\phi_0} + \sum_m \delta n_m \cdot \cos(m \cdot \phi + \alpha_m) \tag{6}$$

Here the first term represents the radial density profile in equilibrium, i.e. in the absence of 3D perturbations, while the second term is a perturbative expansion which takes into account the toroidal dependence introduced by the 3D perturbations. The term δn_m represents the amplitude of the density perturbations associated to the toroidal spectral component m. Since we assume small "rigid" radial shifts of the kinetic profiles i.e. without changes in the profiles shape, we can approximate these as:

$$\delta n_m \sim \left.\frac{\partial n_b}{\partial R}\right|_{R_0} \cdot \xi_m^{pl} \tag{7}$$

where ξ_m^{pl} represents the amplitude of the toroidal component m of the plasma boundary radial displacement induced by the 3D perturbations. We now expand the first term in Eq.6 by considering small deviations from a central R_0 of ξ_{FI}, which represent changes in the radial birth location of the lost ions reaching FILD due to the MP induced orbit displacement:

$$\begin{aligned} n_b(R)|_{\phi_0} = n_b(R_0 + \xi_{FI})|_{\phi_0} = \\ n_b(R_0)|_{\phi_0} + \left.\frac{\partial n_b}{\partial R}\right|_{R_0} \cdot \xi_{FI} + \mathcal{O}(\xi^2) \end{aligned} \tag{8}$$

where we neglect terms of second and higher order in ξ_{FI}. Now, we know that the MP induced fast-ion orbit displacement is a function of the toroidal coordinate, so we make the following expansion:

$$\xi_{FI}(\phi) = \sum_l \xi_l^{FI} \cdot \cos(l\phi + \beta_l) \quad (9)$$

Bringing all together we are left with:

$$n_b(\phi, R) = n_b(R_0, \phi_0) + \left.\frac{\partial n_b}{\partial R}\right|_{R_0} \cdot \sum_l \xi_l^{FI} \cdot \cos(l\phi + \beta_l) + \left.\frac{\partial n_b}{\partial R}\right|_{R_0} \cdot \sum_m \xi_m^{pl} \cdot \cos(m\phi + \alpha_m) \quad (10)$$

Here, the first term is proportional to the FILD signal in the equilibrium case, i.e. considering an axisymmetric magnetic equilibrium and axisymmetric kinetic profiles. The second term represents the modulation of the birth density at the position of the lost ions to FILD due to the MP induced orbit displacement. The third term represents the modulation of the birth density at the position of the lost ions to FILD due to the 3D plasma boundary displacements. Note that, in general $\alpha_l \neq \beta_m$, since the phase due to both modulations can be different, and that we have only considered the partial derivatives with respect to the radial coordinate, following the same arguments as in the Appendix of [37].

Taking $\partial n_b/\partial R$ as a common factor, using Eq.5 and assuming that the proportionality constant which links the ion loss rate at FILD to the ion birth profile is independent from the radial and toroidal coordinates, we are left with:

$$\left.\frac{n_b}{\nabla n_b}\right|_{R_0} \cdot \left[\frac{F - F_0}{F_0}\right] - \sum_m \xi_m^{pl} \cdot \cos(m \cdot \phi + \alpha_m) = \sum_l \xi_l^{FI} \cdot \cos(l \cdot \phi + \beta_l) \quad (11)$$